Climate Dynamics
https://doi.org/10.1007/s00382-019-04864-4

Changes of MJO propagation characteristics under global warming

Jingxuan Cui[1] · **Tim Li**[1,2]

Received: 7 November 2018 / Accepted: 18 June 2019

Abstract
The change of Madden–Julian Oscillation (MJO) propagation and periodicity characteristics under global warming is investigated using two selected CMIP5 models. It is found that the MJO period tends to be shorter, while its eastward propagation tends to be accelerated. Meanwhile the main MJO activity center shifts eastward toward the central equatorial Pacific. Two factors are possibly responsible for the increased eastward phase speed of the MJO. The first is attributed to the increase of atmospheric static stability that accelerates equatorial Kelvin wave speed. The second is attributed to the increase of zonal asymmetry of MJO-scale moist static energy (MSE) tendency, which is contributed to the combined effect of anomalous circulation and mean MSE gradient. A theoretical framework is constructed to understand the relative role of anomalous heating and mean static stability changes in determining MJO-scale circulation change. It is found that their effect is phase dependent. During the initial warming phase the circulation change is primarily controlled by the heating change, whereas during the later warming phase it is primarily controlled by the static stability change. The eastward shift of the main MJO activity center is possibly caused by the occurrence of an El Niño-like mean SST change and associated vertical overturning circulation change in the tropical Pacific.

Keywords Global warming · MJO future projection · MSE tendency asymmetry · Eastward phase propagation

1 Introduction

The Madden–Julian Oscillation (MJO) is the dominant mode of intraseasonal variability in the tropics (Madden and Julian 1972). It is characterized by a planetary zonal scale and slow eastward propagation along the equator (Lau and Chan 1986; Li and Zhou 2009), a horizontal pattern of Kelvin–Rossby wave couplet (Wang and Li 1994; Hendon and Salby 1994), a free-atmospheric first baroclinic mode vertical structure (Wang and Rui 1990), and a phase leading of boundary layer convergence (Li and Wang 1994) and moisture (Hsu and Li 2012). After initiated in the western equatorial Indian Ocean (Zhao et al. 2013), MJO convective envelope moves eastward across the warm pool and remotely impacts climate over Asian and Australian continents (Hong and Li 2009; Lau and Waliser 2011). Westerly wind burst associated with the MJO may trigger ENSO events through induced equatorial ocean waves (Lengaigne et al. 2004; Chen et al. 2017).

The MJO is a major predictability source for extended-range (10–30 days) forecast (Hsu et al. 2014; Zhu et al. 2015). Although its main convective activity is confined in the tropics, the MJO may exert a great impact on global circulation. Many of the current state-of-art climate models, however, have difficulty in simulating the eastward propagation of the MJO (e.g., Jiang et al. 2015). The model bias is likely attributed to a failure to reproduce stratiform clouds in the upper troposphere in the rear of the MJO deep convection (Wang et al. 2017).

Given that the MJO exerts a great impact on extreme weather events such as tropical cyclones (Fu et al. 2007; Bi et al. 2015; Diao et al. 2018), it is important to understand how the MJO characteristics change under global warming. By diagnosing the output of a global coupled

✉ Tim Li
timli@hawaii.edu

[1] Key Laboratory of Meteorological Disaster, Ministry of Education (KLME)/Joint International Research Laboratory of Climate and Environmental Change (ILCEC)/ Collaborative Innovation Center on Forecast and Evaluation of Meteorological Disasters (CIC-FEMD), Nanjing University of Information Science and Technology, Nanjing, China

[2] International Pacific Research Center and Department of Atmospheric Sciences, School of Ocean and Earth Science and Technology, University of Hawaii at Manoa, Honolulu, HI 96822, USA

Published online: 25 June 2019

model with A1B warming scenario, Liu et al. (2013) showed that the amplitude of the MJO would increase. The strengthening of the MJO intensity was thought to be caused by the advection of anomalous moist static energy by the mean vertical velocity (Arnold et al. 2015) or the enhancement of nonlinear wind-induced surface heat exchange (WISHE). The latter is responsible for the increase in surface moisture (Liu et al. 2013). The uneven increase in tropical SST under global warming may modulate the mean state and thus MJO change (Maloney and Xie 2013). Thus, the change of mean state in SST may be a fundamental factor for the MJO change. Note that a significant effect on the SST change is the ENSO, but Hendon et al. (1999) concluded that the year-to-year variation of MJO intensity is uncorrelated with ENSO. In contrast, Liu et al. (2016) pointed out that MJO intensity is controlled by SST anomalies, with the explanation of strong (weak) eastward-propagating MJOs happen during warm (cold) episodes in the central equatorial Pacific.

As for the changes of MJO propagation characteristics under global warming, some previous studies showed a robust increase in the phase speed of the MJO (Arnold et al. 2013, 2015; Chang et al. 2015; Adames et al. 2017a). Consistent with the acceleration of the phase speed, a shift of the MJO spectrum peak toward higher frequencies was found as SST increases in the super parameterized Community Atmosphere Model (SP-CAM) (Arnold et al. 2013). Chang et al. (2015) also reported an increase in the frequency of the MJO spectral power in the European Centre Hamburg Model, version 5, Snow–Ice–Thermocline (ECHAM5-SIT) model. Adames et al. (2017b) and Rushley et al. (2019) attributed the increase of the phase speed in a warmer climate to enhanced horizontal moisture advection due to the increase of mean meridional moisture gradient and the decrease of zonal wavenumber, the latter of which is partially offset by the lengthening of convective moisture adjustment timescale and the increase in gross dry stability.

In this study, we will emphasize the change of the MJO periodicity and propagation characteristics and expound possible mechanisms behind these changes. Our strategy is to first choose the best models from a group of CMIP5 (the Coupled Model Intercomparison Project, Phase 5) models from the RCP 8.5 scenario and then diagnose the output of these models. The rest of this paper is organized as following. In Sect. 2, data and methods are introduced. The comprehensive evaluation of MJO main characteristics in a group of the CMIP5 models is described in Sect. 3. In Sect. 4 we examine the MJO propagation characteristics under different warming phases. In Sect. 5, we further diagnose the model mean state changes and propose physical mechanisms responsible for the change of the MJO behavior. Finally, a conclusion is given in the last section.

2 Data and methods

2.1 Datasets

The observed daily Outgoing Longwave Radiation (OLR) dataset (Liebmann and Smith 1996) with the period of 1979–2005 from National Oceanic and Atmospheric Administration (NOAA) is used in this study. In addition, the reanalysis dataset from the National Centers for Environmental Prediction/National Center for Atmospheric Research (NCEP/NCAR) version I (Kalnay et al. 1996) for the same period as the OLR is used. All the data above have a 2.5° by 2.5° latitude–longitude grid. Multiple CMIP5 model datasets in historical runs and Representative Concentration Pathway 8.5 (RCP8.5) simulations are used for estimating the MJO characteristics changes. The model datasets are all changed into a resolution of $2.5° \times 2.5°$, with a daily interval. The data periods for the historical runs and RCP8.5 simulations are 1950–2005 and 2006–2100 respectively.

2.2 Methods

As global warming began from the industrial revolution, we select the global mean surface temperature during 1860–1880 as a reference temperature level. To understand how the MJO behavior may change under different warming intensity, the entire analysis period of 1860–2100 is separated into three phases: 1 °C warming, 2 °C warming and 4 °C warming phase. The time span of each phase is considered as the period spanning from 0.5 °C below to 0.5 °C above the specified warming temperature (e.g., the 1 °C warming phase is taken as a period from 0.5 °C warming to 1.5 °C warming).

A wavenumber-frequency spectral analysis method developed by Wheeler and Kiladis (1999) is used to isolate the MJO signal. With this method, a given field that is the function of time and longitude can be transferred into a wavenumber and frequency domain for both eastward and westward propagating waves (e.g., Wheeler and Kiladis 1999; Roundy and Frank 2004). Consequently, the space–time characteristic of this wave component can be determined quantitatively. Through the Wheeler–Kiladis space–time diagram derived from daily observed OLR data for the period of 1979–2005, a domain covering the period of 20–100 days and zonal wavenumber 1–5 can be considered as the MJO component for this period. Using this wavenumber-frequency analysis method, the eastward-propagating MJO signal can be isolated from the original daily data.

To evaluate the model capability in simulating the MJO, a Real-time Multivariate MJO (RMM) index (Wheeler

and Hendon 2004) is employed. Firstly a 20 to 100-day Lanczos band-pass filter is employed to the original daily data for the period of 1979–2005. Then the RMM index can be obtained by applying a multi-variable Empirical Orthogonal Function (EOF) analysis to OLR and 850 hPa and 200 hPa zonal wind fields averaged over the equatorial region (15°N–15°S). It is the time series of the leading pair of principal components of the EOF modes that determine the RMM index. This index can be used to describe the longitudinal location and intensity of the MJO at a given time.

The RMM index is used as a criterion for selecting good models in the MJO simulations by comparing with the observed counterpart. While the wavenumber-frequency spectrum analysis result is primarily used to analyze the change of MJO periodicity under different warming phases, a lead-lag correlation between the OLR anomaly and the intraseasonal OLR time series at a given location is calculated to analyze the change of eastward phase propagation speed of the MJO.

Because tropical intraseasonal oscillations (ISOs) exhibit pronounced seasonality in its intensity, frequency and movement (e.g., Wang and Rui 1990; Li 2014), one needs to reveal ISO characteristics in boreal winter and summer separately. In this paper we focus on the analysis of boreal winter ISO (from November to April).

3 Evaluation of MJO present-day characteristics in selected CMIP5 models

Thirteen CMIP5 models (i.e., ACCESS1.0, CNRM-CM5, CSIRO-Mk3.6.0, GFDL-ESM2M, INM-CM4, IPSL-CM5A-LR, IPSL-CM5A-MR, IPSL-CM5B-LR, MIROC-ESM, MIROC-ESM-CHEM, MPI-ESM-LR, MRI-CGCM3 and NorESM1-M) were available in our serve and used for this study. To select the best models from them, we first compared the model simulated MJO from their historical runs with the observation. First, the MJO-scale power spectrum from each model is examined and compared with the observed counterpart. The wavenumber-frequency spectrum diagram of 20 to 100-day, 1 to 5-wavenumber filtered OLR from the observation shows the MJO concentrates on wavenumber 1–3 and period of about 40–80 days, but the model OLR anomalies vary.

To quantitatively measure the model spectrum characteristics, the power spectra of the anomalous OLR as a function of period averaged over wavenumber 1–3 are examined. It is noted that some models show proper amplitude compared to the observation, while others exhibit much a weaker intensity. By separating the 13 models into two groups, a strong group (with the proper amplitude compared to the observation) and a weak group (with amplitude much less than the observation) (seen in Fig. 1). The following six models in the strong group (CNRM-CM5, CSIRO-Mk3.6.0, IPSL-CM5B-LR, MPI-ESM-LR, MRI-CGCM3 and NorESM1-M) are selected for further evaluation.

Secondly, the dominant periodicity in the power spectrum is examined. It is noted that in the strong group three models (CNRM-CM5, CSIRO-Mk3.6.0 and MRI-CGCM3) exhibit a spectrum peak near the period of 60 days, similar to the observation, whereas the other three models have either too short or too long periods. For example, IPSL-CM5B-LR has a peak near the period of 38 days, whereas MPI-ESM-LR and NorESM1-M have a peak at the 80-day period. Thus, by comparing modeled and observed MJO periodicity, we concluded that IPSL-CM5B-LR, MPI-ESM-LR and NorESM1-M reproduced unsatisfactory space–time features, and thus are excluded from the subsequent model analysis.

Because the objective of this study is to project future change of MJO activity under global warming, the model's performance in capturing MJO trends in recent decades

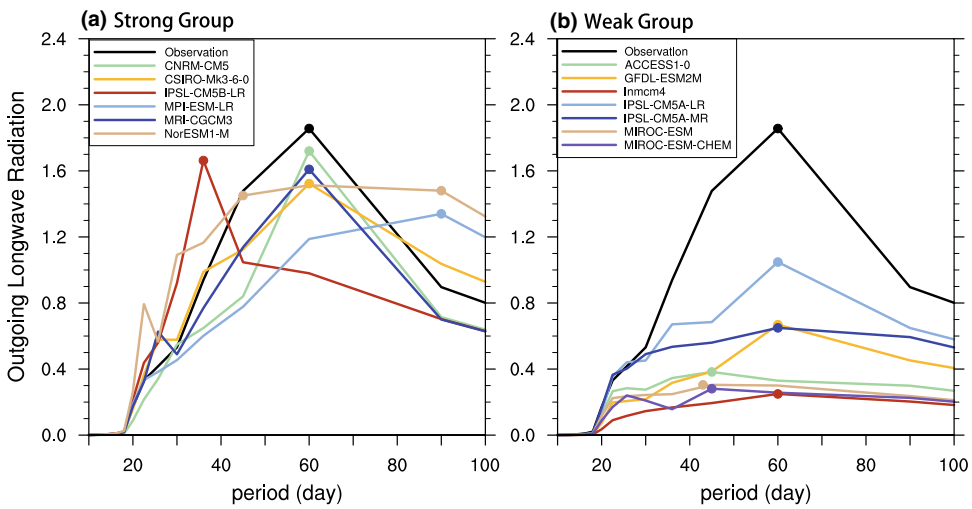

Fig. 1 Power spectra of space–time filtered OLR (unit: W/m^2) averaged in zonal wave numbers 1–3 based on the observation and model simulations of **a** strong group and **b** weak group for 1979–2005

(1979–2005) is further evaluated. Both the trends of the RMM index and the global mean surface temperature during the period are calculated. To remove the influence of the interannual variation, a 9-year running mean is employed on the time series (shown in Fig. 2). Note that while the three selected models exhibit a similar positive trend for global mean surface temperature, a negative trend for RMM appears in the CNRM-CM5 model, which is opposite to the observed and the other two models. Because of this consideration, the CNRM-CM5 model is excluded from the subsequent analysis. As a result, only two best models, MRI-CGCM3 and CSIRO-Mk3.6.0, are selected for the global warming projection.

4 Projected MJO characteristics changes under global warming

4.1 Phases of global warming

To reveal how the MJO behavior changes under different warming strength, the global mean surface air temperature is used to characterize various phases of global warming. As described in Sect. 2, the global mean surface air temperature averaged during 1860–1880 is regarded as a reference temperature. The entire analysis period is divided into three warming phases: 1 °C, 2 °C and 4 °C warming phase. Each phase consists of a period spanning from 0.5 °C below to 0.5 °C above (Fig. 3). For example, the 1 °C warming phase is taken as the period spanning from 0.5 °C warming to 1.5 °C warming.

As the global mean temperature evolves differently in different models, we calculate the MJO characteristics based on 1, 2 and 4 °C warming phases of each model. Then the MJO characteristics are averaged in each corresponding warming phase. The so-generated results are more credible than the result based on the averaged temperature time series of the two models. The periods of each of the specific warming phases for the two models are listed in Table 1.

Because the present-day climate is approximately at 1 degree warming phase relative to the temperature during 1860–1880, in the following, we will primarily examine how the MJO activity changes in future 2 °C and 4 °C warming phases and regard the present-day climate as a reference state.

4.2 Changes in MJO characteristics

4.2.1 Changes in periodicity

Figure 4 shows the wavenumber-frequency spectra of the space–time filtered OLR and 850 hPa zonal wind fields during the three warming phases for the individual model. It is noted that for both the OLR and zonal wind fields the main power appears shifting toward the higher frequency with the increase of global warming. This implies that the MJO becomes more energetic toward a shorter period around 20–40 days.

To quantitatively measure the frequency shift, one may calculate the accumulated spectrum for higher (20 to 40-day) and lower (40 to 80-day) frequency bands. Figure 5 shows that with the increase of global mean temperature, the energy of the higher-frequency component of the MJO increases in both the models while the energy of the lower-frequency component decreases (or changes little). The values of percentage increase of power of the higher frequency bands are shown in Table 2. For instance, the increase rate of higher-frequency component from 1 to 2 °C warming phase is about 26.7% for MRI-CGCM3 and 2.5% for CSIRO-Mk3.6.0. Such a rate increases to 46.2% and 6.6% respectively while the global mean temperature reaches 4 °C warming phase. Therefore it is concluded that the energy of higher-frequency component of the MJO always increases under global warming. The result implies that the MJO period will be shortened with global warming.

4.2.2 Changes in propagation speed

The eastward phase propagation speed of the MJO can be estimated by correlating the OLR anomaly field averaged over 15°S–15°N onto a reference OLR time series over a specific location. Figure 6 shows the lagged time-longitude diagrams of the OLR anomaly at 1 °C, 2 °C and 4 °C warming phases when the reference point is set at Maritime Continent (115°E–125°E, 5°S–15°S). All three panels display clear eastward phase propagation of the MJO. In the figure, day 0 represents the time when the MJO reaches a peak phase over the Maritime Continent longitudes.

The eastward phase propagation speed can be estimated based on the slope of the maximum correlation coefficient (denoted by black arrows in Fig. 6). Our calculation shows that the eastward phase speed becomes faster with the increase of global warming. The average phase speed is increased from 3.6 m/s in the 1 °C warming phase to 3.9 m/s in the 2 °C warming phase and further to 4.1 m/s in the 4 °C warming phase (Table 3). The increase rate is about 6%. Such an increase in the eastward phase speed under global warming is consistent with the decrease of periodicity discussed in the previous subsection.

4.2.3 Changes in activity center

The main activity center of the MJO at 1 °C warming phase is confined south of the equator over the eastern Indian Ocean and Maritime Continent longitudes, as seen from the map of standard deviation of the space–time filtered

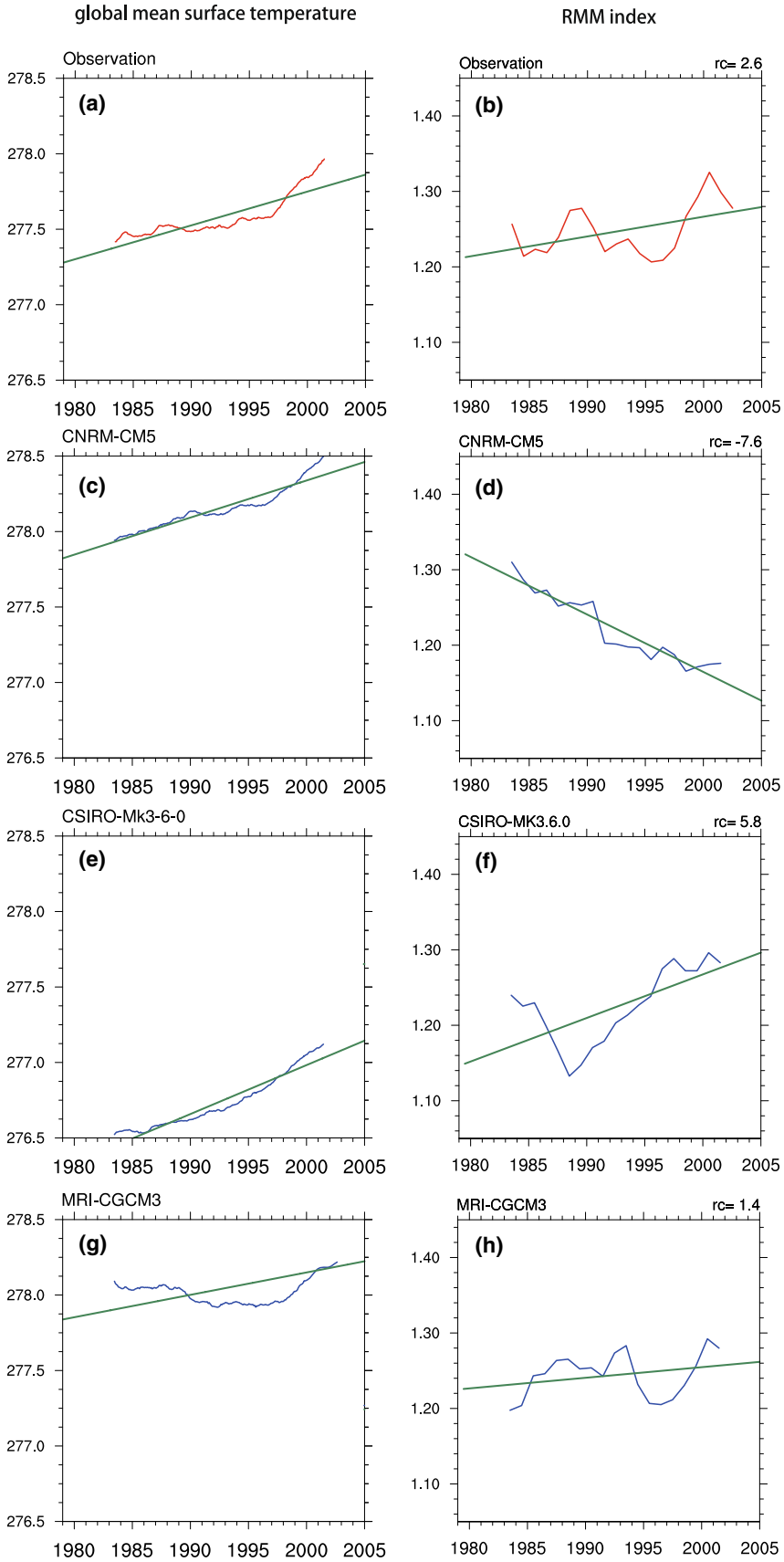

Fig. 2 Time series with 9-year running mean of (left) global mean surface temperature and (right) the RMM indices calculated from the (red) observation and (blue) three selected models for the periods of 1979–2005. The green lines and the numbers (unit: 10^{-5} day^{-1}) at top-right corner of each panel represent the linear trends

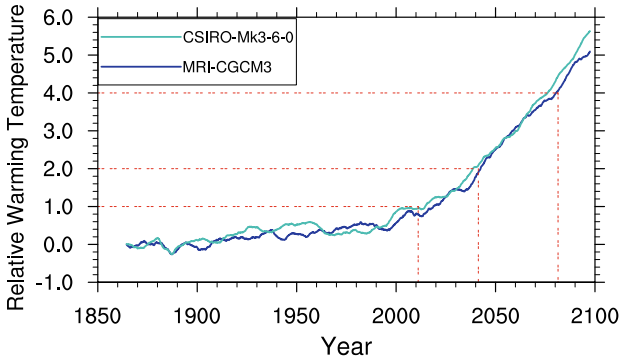

Fig. 3 Time series of global mean surface air temperature (unit: °C) departed from 1860 to 1880 reference mean state, as simulated by MRI-CGCM3 and CSIRO-Mk3.6.0 models

Table 1 Time period for 1 °C, 2 °C and 4 °C warming phases based on global mean surface air temperature time series simulated by MRI-CGCM3 and CSIRO-Mk3.6.0

Warming	Period	
	MRI-CGCM3	CSIRO-Mk3.6.0
1 °C (0.5–1.5)	1991.11.25–2028.10.15	1995.04.01–2031.08.31
2 °C (1.5–2.5)	2036.08.15–2050.06.01	2031.09.01–2049.06.30
4 °C (3.5–4.5)	2067.10.30–2086.03.15	2066.11.01–2082.03.15

OLR field (Fig. 7a, d). With the increase of the global mean surface temperature, the maximum activity center gradually shifts eastward towards the western and central tropical Pacific (Fig. 7b, c, e, f).

The difference maps in Fig. 7b, c, e, f imply that with a continuous increase of global warming, the main convective branch of the MJO can penetrate further eastward into the central Pacific (near 150°W). This is likely attributed to the occurrence of Central Pacific-type El Niño-like warming in the mean climate state in the models. More discussion on the physical cause will be presented in Sect. 5.

5 Mechanisms for MJO characteristics changes

Because large-scale mean circulation has an important influence on the development of the MJO, we first diagnose the change of the mean state field. In the following, we will analyze the changes of climatological mean SST, lower tropospheric water vapor and wind, precipitation, vertical overturning circulation and potential temperature fields in each of the warming phases. All the mean state analysis is considered for the boreal winter season. Given that mean state changes simulated by the two selected models bear great similarity, in the following only the ensemble mean results are presented.

Relative changes of mean SST from 1 °C to 2 °C and 4 °C are displayed in Fig. 8. While the warm pool in the present-day climate is confined in the western Pacific (Fig. 8a), a Central Pacific-type El Niño-like warming pattern appears in the equatorial Pacific (Fig. 8b, c). The amplitude of the mean SST change increases from 2 to 4 °C warming phase as expected. The maximum warming center appears extending eastward gradually from 160°E to east of 180°E.

The rising of the mean state SST in the central equatorial Pacific leads to the increase of surface latent heat flux and precipitation in situ (Fig. 9). As one can see from Fig. 9, with global warming, precipitation significantly increases in the western-central equatorial Pacific, and has a consistent distribution with SST change shown in Fig. 8. The increased surface evaporation caused by the warming results in an increase in low-level water vapor (Fig. 10), which benefits for the increase in precipitation. The enhanced precipitation may further increase column water vapor through enhanced ascending motion and low-level convergence, which causes more water vapor to be transported upward. Such a background change provides more favorable conditions for the development and enhancement of the MJO, and is responsible for the overall increase of the MJO intensity and the eastward extension of MJO convective activity under global warming.

The eastward shift of precipitation and moisture can be also inferred from the change of the Walker circulation along the equatorial Indo-Pacific. Figure 11 illustrates the zonal-vertical cross section of the vertical overturning circulation averaged over 15°S–15°N. In the present-day climate (Fig. 11a), a strong ascending motion appears over the Maritime Continent (near 120°E), while descending motion occurs over the eastern Pacific. With global warming, significant enhanced ascending anomalies occur over the central equatorial Pacific around the dateline, while significant reduction of ascending motion appears over the Maritime Continent. Such a vertical overturning circulation change is consistent with the Central Pacific-type El Niño-like warming mean state change and associated precipitation and moisture variations. It is the combined (moisture, SST and ascending motion) mean state change that causes the eastward shift of maximum MJO activity center.

The shortening of the MJO periodicity under global warming is closely related to the acceleration of MJO eastward phase propagation speed. This is because for given the same zonal wavenumber, phase speed depends on frequency. An increase of MJO frequency (or a reduction of MJO period) leads to an increase of phase speed. In order to explore physical mechanisms responsible for the change of MJO phase speed, we conducted a diagnostic analysis of the mean-state stability change under each warming phase, by

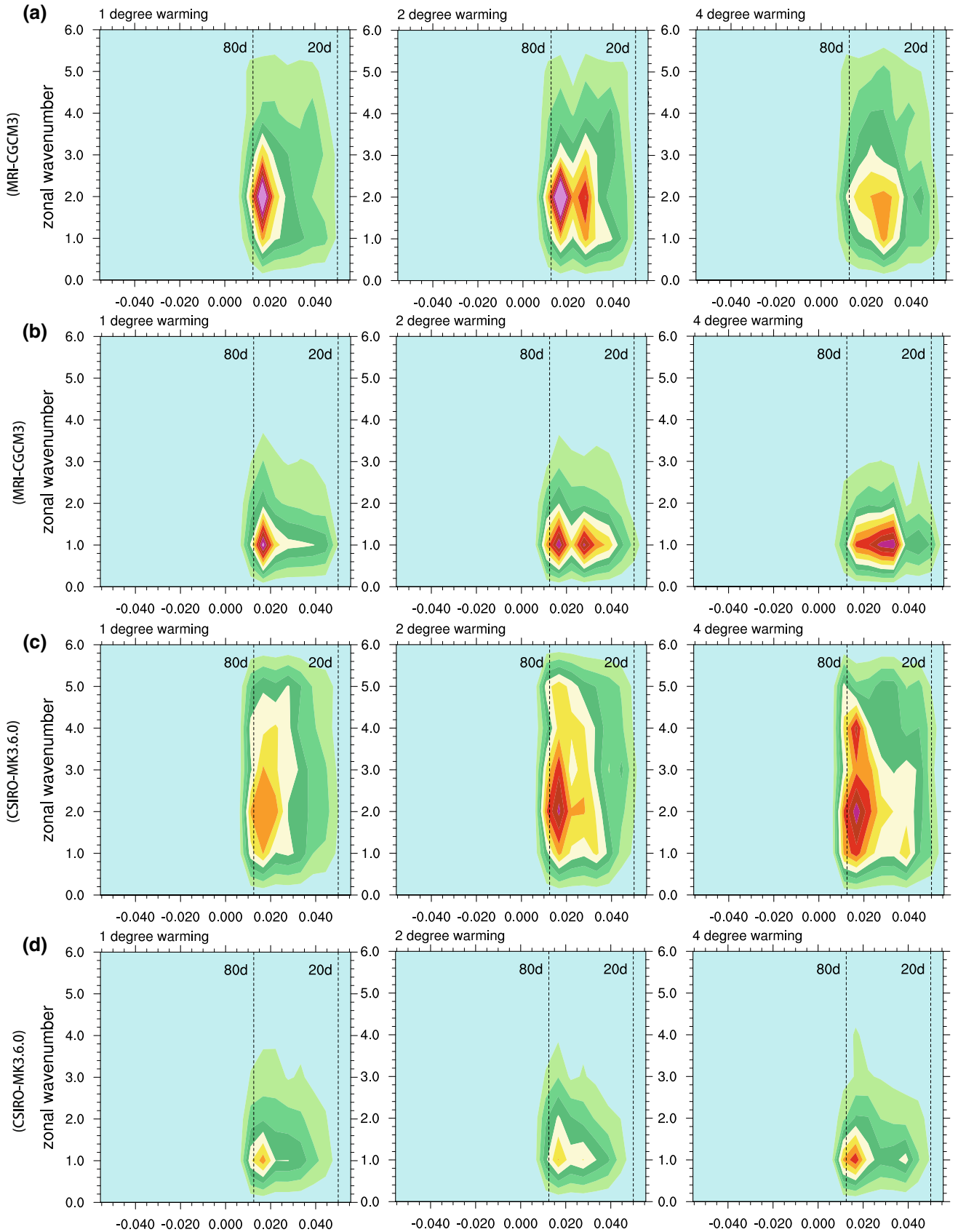

Fig. 4 Wavenumber-frequency spectra of space–time filtered **a**, **c** OLR (unit: W/m^2) and **b**, **d** 850 hPa zonal wind fields (unit: m/s) in (column 1, 2 and 3) 1 °C, 2 °C and 4 °C warming phases for MRI-CGCM3 and CSIRO-Mk3.6.0

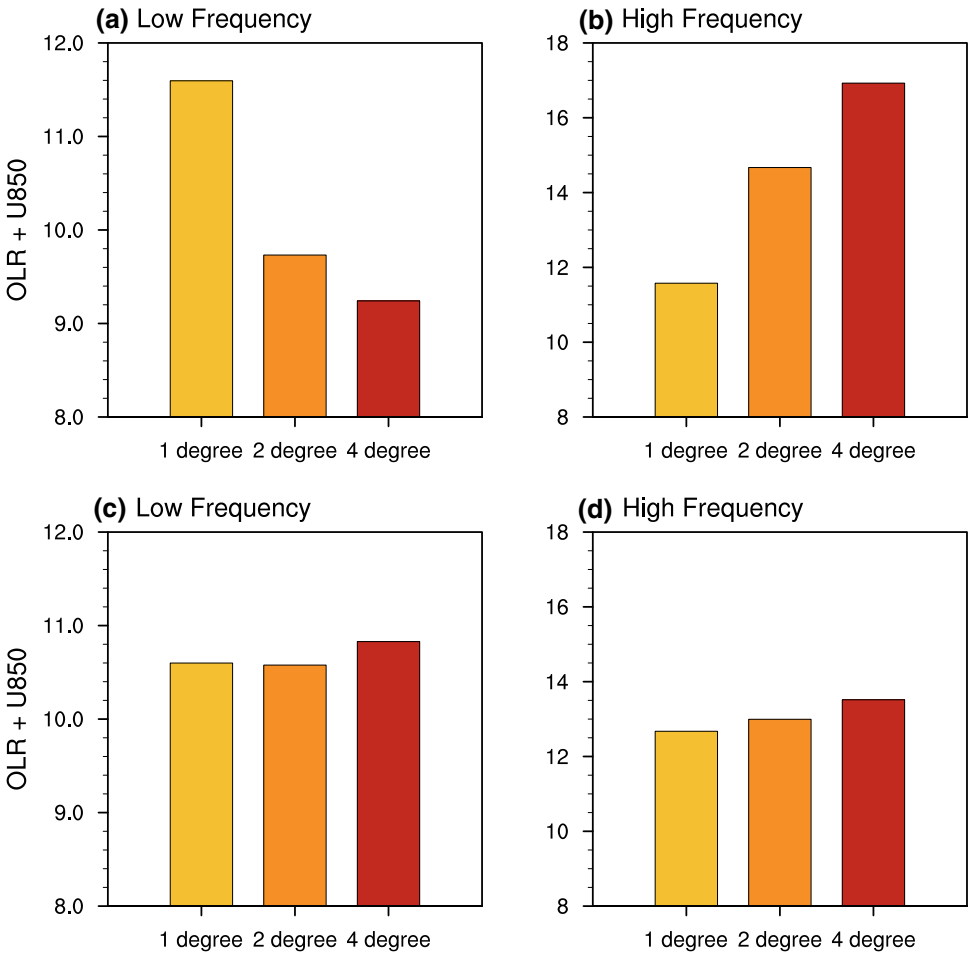

Fig. 5 Power spectra of combined standardized space–time filtered OLR accumulated over zonal wave numbers 1–3 and 850 hPa zonal wind accumulated over zonal wave numbers 1–2 in 1 °C, 2 °C and 4 °C warming phases for (top) MRI-CGCM3 and (bottom) CSIRO-Mk3.6.0. The left panels describe the change of the lower-frequency component, with solid-fill bars representing the averages of the 40–80 days band. The right panels describe the change of the higher-frequency component, with bars representing the averages of the 20–40 days band

Table 2 Percentage increase of higher-frequency power spectrum components of combined MJO-scale OLR and 850 hPa zonal wind anomalies under global warming for MRI-CGCM3 and CSIRO-Mk3.6.0

	From 1 to 2 °C (%)	From 1 to 4 °C (%)
MRI-CGCM3	26.7	46.2
CSIRO-Mk3.6.0	2.5	6.6

analyzing the vertical profiles of mean potential temperature in the tropics (averaged over 15°S–15°N).

Figure 12 shows the difference in potential temperature vertical profiles between 1 and 2 °C warming phase and between 1 and 4 °C warming phase. A marked increase of potential temperature appears at 250 hPa for each of the warming phases, compared to the reference phase (i.e., 1 °C warming phase). The result indicates that as the globe continues warming, upper tropospheric temperature increases at a much larger rate than the temperature in the lower troposphere. As a consequence, the atmosphere becomes more and more hydrostatically stable. The increase of the atmospheric static stability can cause the acceleration of internal gravity waves and thus equatorial Kelvin waves. As the MJO may be regarded as a convectively coupled Kelvin wave (Wang 1988) or a Kelvin–Rossby wave couplet (Wang and Li 1994), the enhanced Kelvin waves may hasten MJO eastward phase propagation (Wang et al. 2018).

In addition, the increase of MJO phase propagation speed under global warming can be explained by the increase of zonal asymmetry of anomalous Moist Static Energy (MSE) tendency (Wang et al. 2017). MSE is defined as $m = c_p T + gz + L_v q$, where T is temperature, z is height, q is specific humidity, c_p is the specific heat at constant pressure ($=1004$ J K^{-1} kg^{-1}), g is the gravitational acceleration ($=9.8$ ms^{-2}), and L_v is the latent heat of vaporization ($=2.5\times10^6$ J kg^{-1}). The column-integrated MSE budget can be written as following:

$$\langle \partial_t m \rangle = -\langle \omega \partial_p m \rangle - \langle \mathbf{V} \cdot \nabla m \rangle + Q_t + Q_r, \quad (1)$$

where angle brackets represent a mass-weighted vertical integral from 1000 to 100 hPa, V is horizontal wind vector,

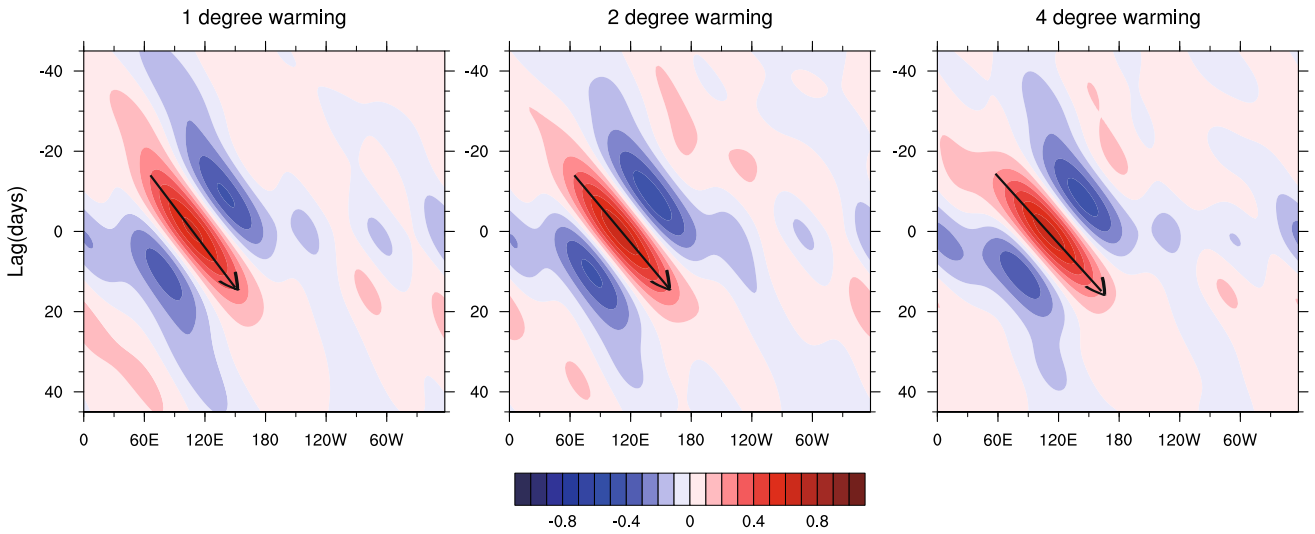

Fig. 6 Longitude–time sections of correlation of anomalous OLR field averaged over 15°S–15°N against space–time filtered OLR averaged over 115°E–125°E, 5°S–15°S in 1 °C, 2 °C and 4 °C warming phases. The black lines indicate the line of the maximum correlation coefficient. The ensemble mean of MRI-CGCM3 and CSIRO-Mk3.6.0 is shown

Table 3 MJO phase propagation speed in 1 °C, 2 °C and 4 °C warming phases

	1 °C	2 °C	4 °C
Propagation speed	303 km/day (3.6 m/s)	322 km/day (3.9 m/s)	341 km/day (4.1 m/s)

and ω is pressure vertical velocity. The left-hand-side term represents MSE tendency, and the terms on right-hand-side represent the vertical and horizontal advection, the sum of surface latent and sensible heat flux, and vertically integrated radiative (including shortwave and longwave) heating rate, respectively.

Figure 13 shows the zonal-vertical distributions of MSE tendency, and Fig. 14 shows the horizontal distribution of column-integrated MSE tendency in 1 °C, 2 °C and 4 °C warming phases, respectively, for MRI-CGCM3 and CSIRO-Mk3.6.0 models. As one can see, there is an obvious east–west contrast in each phase and model, and an obvious increase of the zonal asymmetry under global warming (seen in Table 4).

According to previous observational and model diagnosis (e.g., Maloney 2009; Jiang et al. 2015; Wang et al. 2017), the dominant term in the MSE tendency zonal asymmetry is horizontal MSE advection. Thus, this term is particularly examined. It is found that the horizontal advection is primarily controlled by the advection of mean MSE by anomalous wind (i.e., $-v'\partial\bar{m}/\partial y$ and $-u'\partial\bar{m}/\partial x$, where a prime denotes the MJO-scale motion and a bar denotes the background mean state). Figure 15 displays the contribution of this term at each warming phase. In both the models, the increase of the asymmetry of MSE tendency is consistent with the increase of anomalous horizontal advection, in particular the anomalous meridional advection (i.e., $-v'\partial\bar{m}/\partial y$).

We further investigate which factor is critical for the increase of the east–west asymmetries of $-v'\partial\bar{m}/\partial y$. Figure 16 shows that the increase of the anomalous meridional wind primarily contributes to the increase of the east–west asymmetry during the initial warming phase (i.e., from 1 to 2 °C), but the increase of the mean MSE gradient is a primary factor for the later warming phase (i.e., from 2 to 4 °C).

The cause of this phase-dependent feature is further explored. Atmospheric circulation response to a specified MJO heating in an equatorial beta-plane may be described by the Gill model with a longwave approximation:

$$\begin{cases} \varepsilon u - \beta y v = -\frac{\partial \emptyset}{\partial x} \\ \beta y u = -\frac{\partial \emptyset}{\partial y} \\ \varepsilon \emptyset + c^2 \nabla \cdot \vec{V} = -a\dot{Q} \end{cases}, \tag{2}$$

where u, v, $\emptyset$ and $\dot{Q}$ represent MJO-scale zonal wind, meridional wind, geopotential and diabatic heating, ε is Rayleigh friction coefficient and c is the first-baroclinic gravity wave speed. Considering a steady-state response at each warming phase and denoting "d" as the change between two warming phases, one may derive the following relation:

$$\frac{dv}{v} = \frac{d\dot{Q}}{\dot{Q}} - A\frac{d\sigma}{\sigma}, \tag{3}$$

where parameter A is a function of atmospheric static stability and characteristic zonal length scale. For detailed derivations of the equation above, readers are referred to the

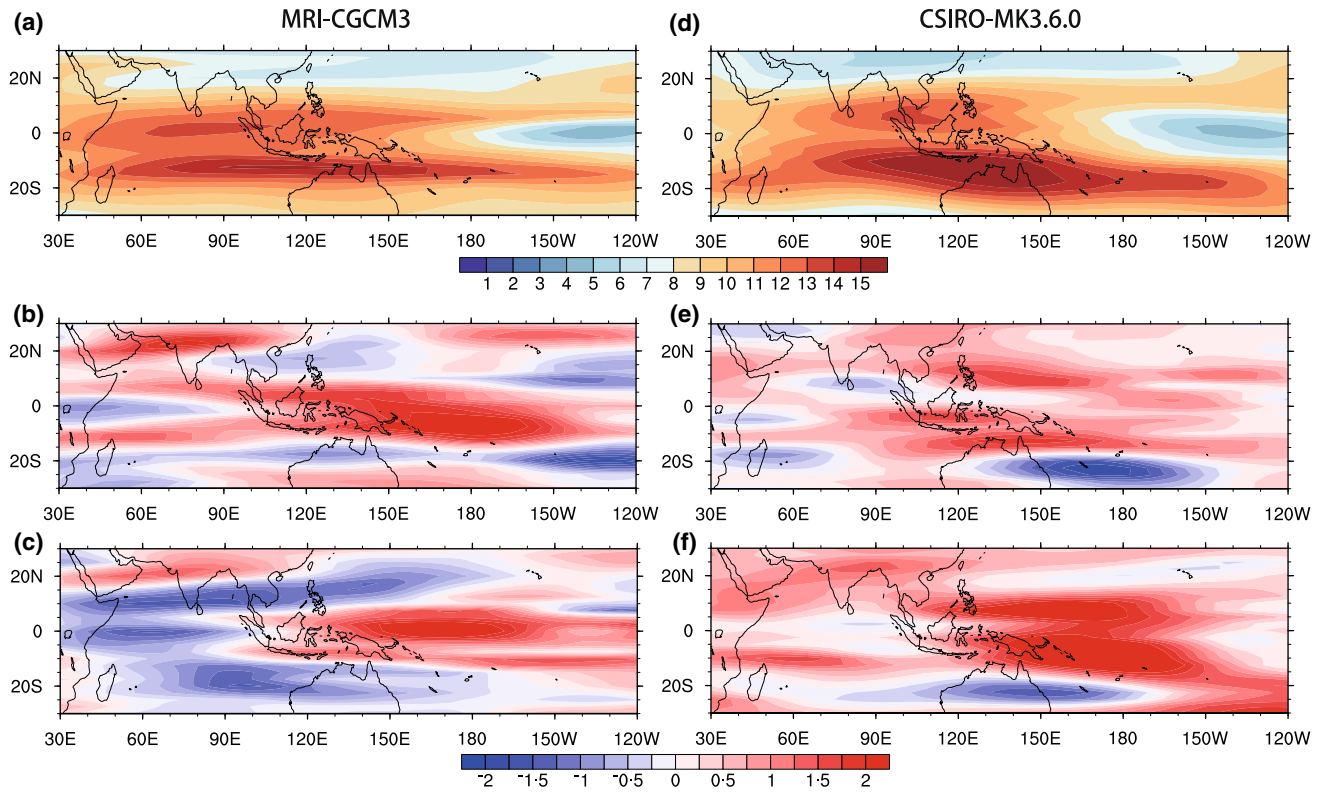

Fig. 7 **a**, **d** Horizontal patterns of standard deviation of space–time filtered OLR (unit: W/m^2) in reference state for MRI-CGCM3 and CSIRO-Mk3.6.0, and their differences **b**, **e** between 2 and 1 °C warming phase and **c**, **f** between 4 and 1 °C warming phase for MRI-CGCM3 and CSIRO-Mk3.6.0 respectively

Appendix. Equation (3) states that the percentage change of MJO-scale meridional wind is determined by the competition of percentage change of diabatic heating ($d\dot{Q}/\dot{Q}$) and percentage change of mean state static stability ($d\sigma/\sigma$). For given the Rayleigh friction coefficient of (1.5 day)$^{-1}$ and characteristic zonal length scale of 1000 km, the change rate of anomalous meridional wind can be estimated quantitatively, given the change rates of MJO-scale diabatic heating ($\dot{Q}$) and mean state static stability (σ). Table 5 shows the calculation results when MJO-scale heating is determined based on the anomalous precipitation regressed onto a reference OLR time series over 115°E–125°E, 5°S–15°S and the static stability is calculated based on the average from 700 to 200 hPa over a large tropical domain (80°E–160°E, 20°S–20°N).

According to Table 5, the percentage increase of MJO-scale heating from 1 to 2 °C is much larger than the percentage change of mean static stability in both the models. As a result, MJO-scale circulation is greatly enhanced. This is in contrast with the later warming phase when the mean static stability increases at a much greater rate than the MJO heating. Consequently, MJO-scale motion merely increases in CSIRO-Mk3.6.0 or even decreases in MRI-CGCM3. The estimated change rates of MJO-scale meridional wind is quite close to the actual rates, suggesting that the proposed framework to isolate the relative roles of mean state static stability change and anomalous heating change is reliable.

The analysis above reveals a phase dependent circulation change characteristic. Different from Adames et al. (2017b) and Rushley et al. (2019) who argued that the increase in static stability would slow down MJO propagation through the reduction of MJO-scale circulation and thus zonally asymmetric MSE tendency, here we argue that it is the competition of anomalous diabatic heating and mean static stability that determines the final outcome of the anomalous circulation. During the initial warming phase (1 °C to 2 °C), the effect of anomalous heating dominates the effect of static stability. The great increase of the anomalous circulation contributes primarily to the increase of zonal asymmetry of the MSE tendency (Fig. 16) and thus the eastward phase speed. During the later warming phase (2 °C to 4 °C), the static stability effect offsets the heating effect. As a result, MJO-scale circulation change plays a minor role. The main contributor to the increase of zonal asymmetry of the MSE tendency arises from the increase of mean meridional moisture gradients (Fig. 16).

An interesting open question is why the rate of anomalous diabatic heating increase in the later warming phase

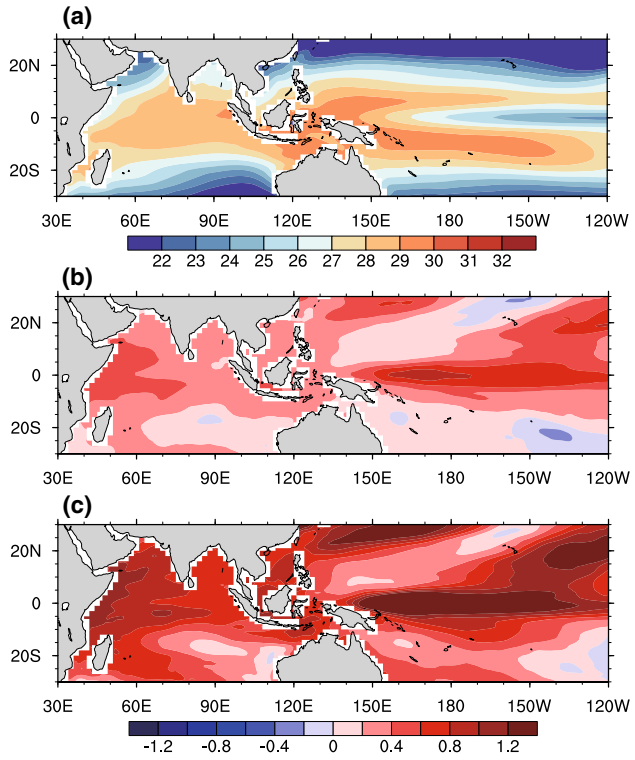

Fig. 8 **a** Horizontal pattern of boreal winter mean SST (unit: °C) in the 1 °C warming reference state, and their differences **b** between 2 and 1 °C warming phase and **c** between 4 and 1 °C warming phase

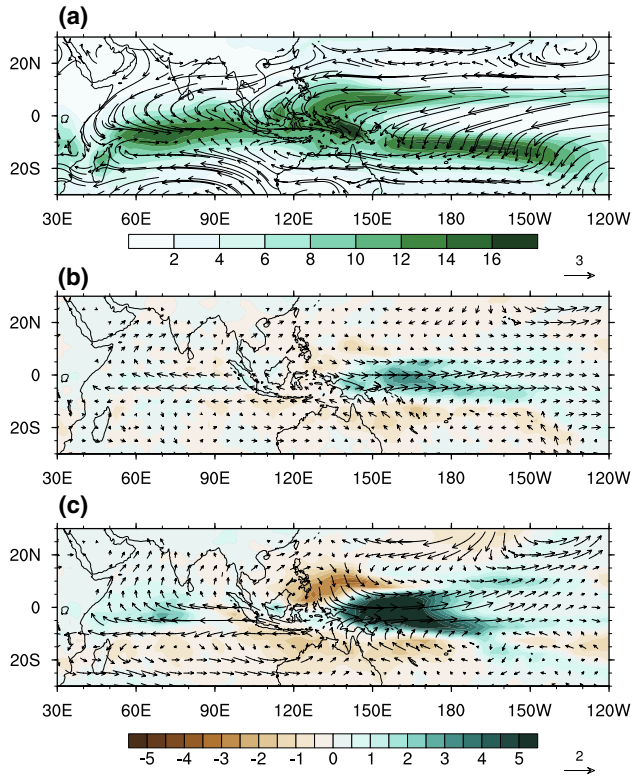

Fig. 9 Same as Fig. 8 except for boreal winter mean precipitation (shading; 10^{-5} kg m^2 s^{-1}) and 850 hPa wind (vector; m/s) fields

is much weaker than that during the initial warming phase in both the models (Fig. 7, Table 5). We speculate that it might be attributed to the El Niño-like mean state SST change in the tropical Pacific. A greater warming in equatorial central-eastern Pacific in the later warming phase promotes a stronger anomalous Walker Circulation that could suppress MJO heating over the Maritime Continent region through reduced background water vapor content.

It is noticed that the increase of meridional gradient of the mean MSE ($\partial\bar{m}/\partial y$) under global warming is primarily attributed to the moisture component (i.e., $L_v q$ term), while the contributions from other terms are small (Fig. 17). The maximum increase of the mean moisture under global warming appears over the equator and such an increase decreases toward higher latitudes. As a result, the meridional gradient of the mean moisture ($\partial\bar{q}/\partial y$) increases in the tropics. This factor alone could lead to the increase of the zonal asymmetry of anomalous meridional MSE advection and thus the acceleration of the MJO eastward phase speed. The increase of MJO-scale circulation, in particular during the initial warming phase, serves as an additional factor to amplify the asymmetric MSE tendency.

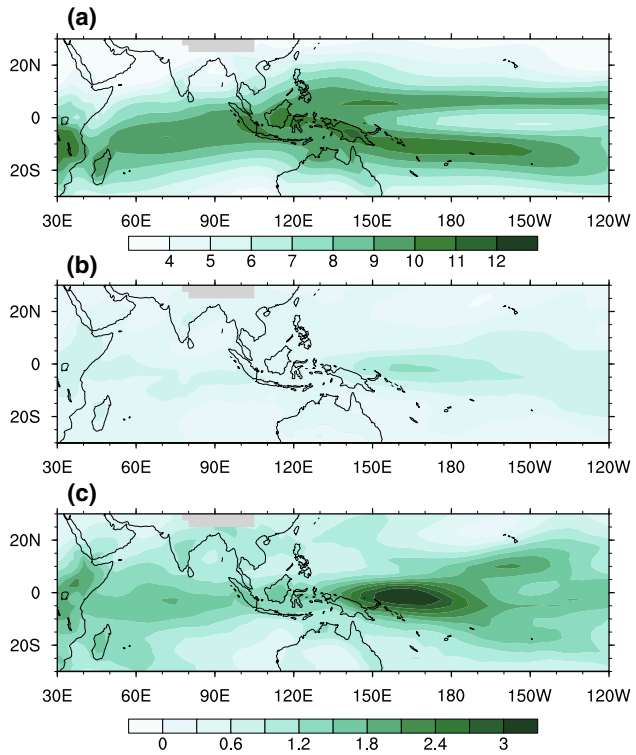

Fig. 10 Same as Fig. 8 except for vertically integrated (850–700 hPa) mean specific humidity (unit: g/kg) field in boreal winter

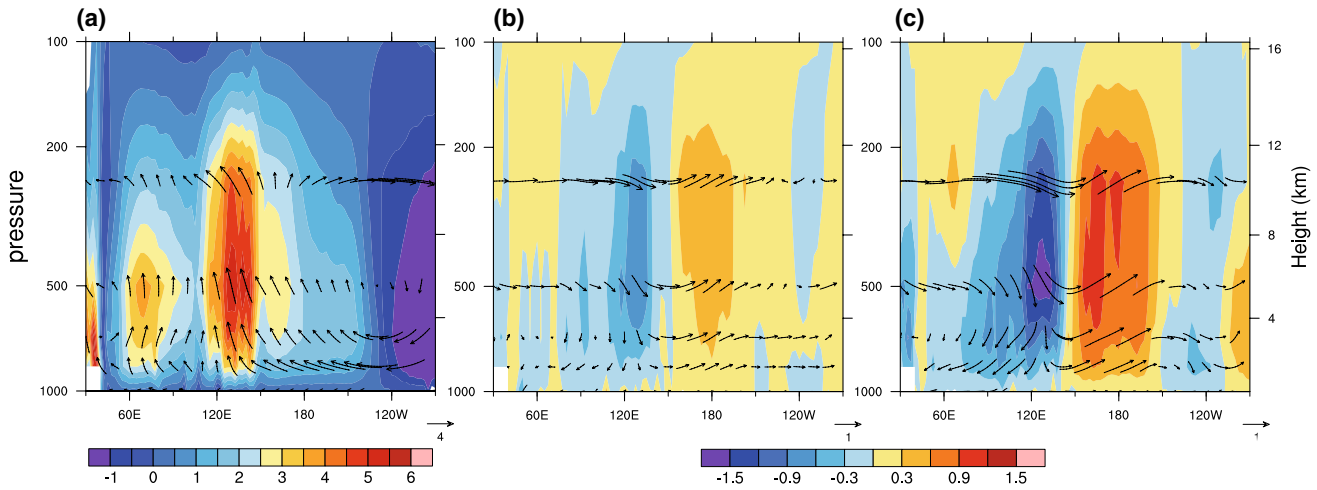

Fig. 11 **a** Zonal-vertical distribution of boreal winter Walker Circulation (unit: °C) in the 1 °C warming reference state, and their differences **b** between 2 and 1 °C warming phase and **c** between 4 and 1 °C warming phase. The vertical p-velocity is shaded (unit: -10^{-2} Pa/s), and has been multiplied by -100 so that positive value represents ascending motion. The unit of zonal wind is m/s

6 Conclusion

By comparing the wavenumber-frequency features of MJO-scale convection and the trend of the RMM index during the period of 1979–2005, we selected two best models (MRI-CGCM3 and CSIRO-Mk3.6.0) from 13 CMIP5 models to investigate the changes of MJO propagation and periodicity characteristics under global warming. It is found that under global warming, MJO becomes more energetic towards a shorter period. The shortening of the MJO periodicity is consistent with a faster eastward phase speed along the equator. On average, the model eastward phase speed increases from 3.6 m/s in the current climate state to 4.1 m/s in a warmer state at the end of twenty-first century.

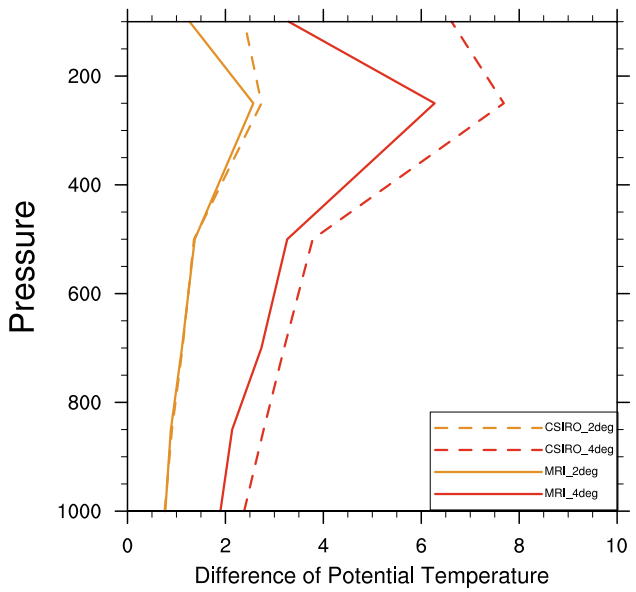

Fig. 12 Vertical profiles of differences of annual mean potential temperature (unit: °C) averaged over global tropics (15°S–15°N) (orange) between 2 and 1 °C warming phase and (red) between 4 and 1 °C warming phase for (solid line) MRI-CGCM3 and (dashed line) CSIRO-Mk3.6.0

Two factors may be responsible for the increased eastward phase speed. On the one hand, an increased atmospheric static stability due to global warming can accelerate equatorial Kelvin waves, which may hasten MJO eastward phase speed as the Kelvin wave component contributes positively to the MJO propagation (Wang et al. 2018). On the other hand, a greater zonal asymmetry of anomalous MSE tendency can accelerate MJO eastward phase speed. Our model diagnosis shows that factor that causes the increase of the zonally asymmetric MSE tendency differs during the initial and later warming phases. It is primarily attributed to the increase of MJO-scale circulation during the initial warming phase and to the increase of the mean moisture gradient during the later phase.

A theoretical framework is developed to reveal the relative roles of the anomalous heating and mean static stability changes in determining the anomalous circulation change. It is found that the net effect is warming phase dependent in both the models. During the initial warming phase, the change of the anomalous circulation is primarily controlled by the change of the anomalous heating. During the later warming phase, the change of the anomalous circulation is primarily controlled by the change of the mean static stability. It is speculated that such a phase dependent feature is caused by the El Niño-like mean SST change.

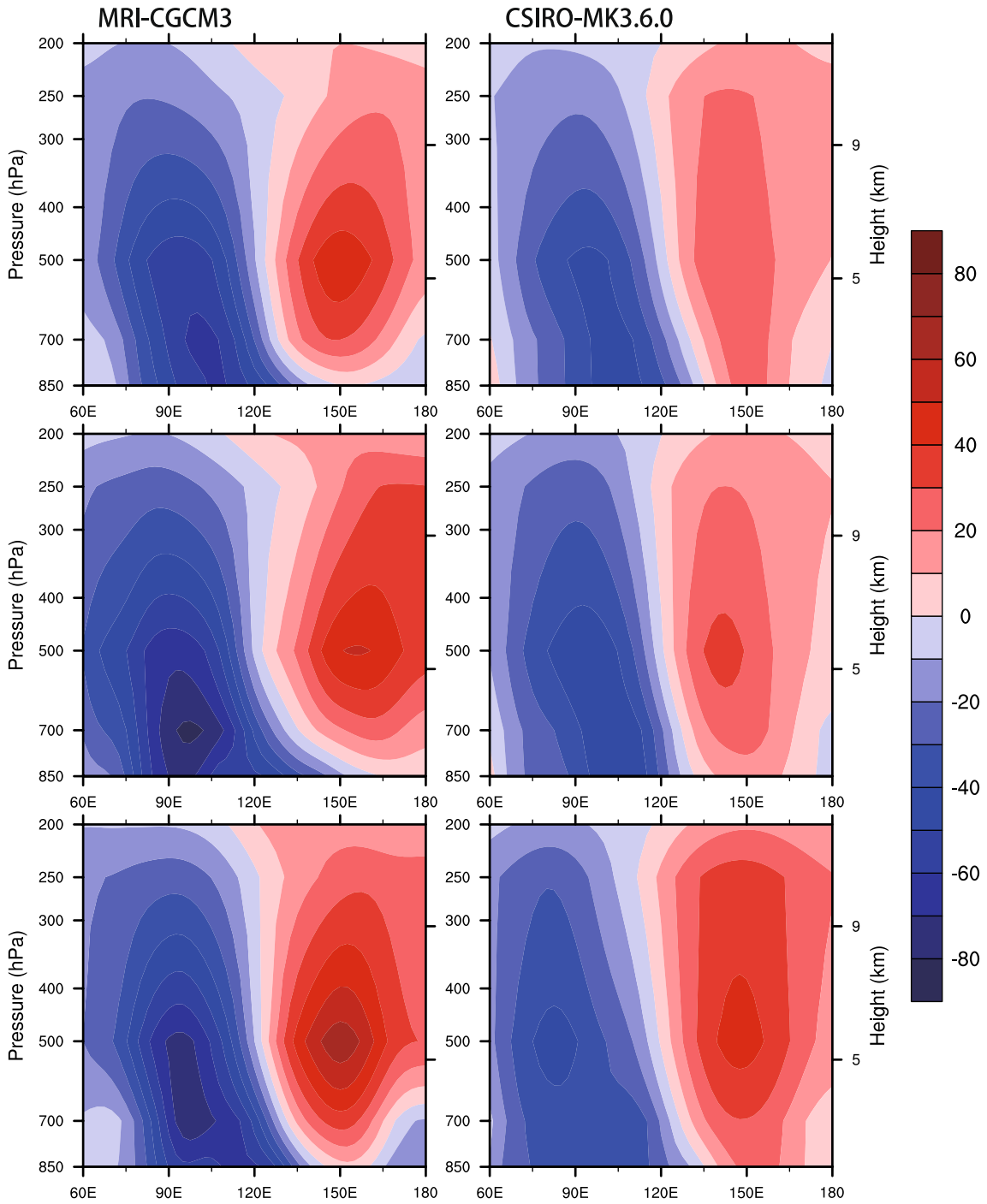

Fig. 13 Zonal-vertical distributions of MSE tendency (unit: $m^2\ s^{-2}\ day^{-1}$) averaged over 20°S–20°N in (row 1, 2 and 3) 1 °C, 2 °C and 4 °C warming phases for (left) MRI-CGCM3 and (right) CSIRO-Mk3.6.0

In addition to the propagation characteristics change, the main MJO activity center tends to shift eastward into the central equatorial Pacific under global warming. The shift is primarily attributed to a Central Pacific-type El Niño-like mean state SST warming pattern in the equatorial Pacific. The maximum warming in the equatorial central Pacific leads to a weakening of the Walker Circulation and an increase of mean moisture in situ due to enhanced surface evaporation and low-level convergence, which provide favorable conditions for MJO development in the region. Therefore the maximum MJO activity center shifts eastward in accompany with the eastward shift of anomalous

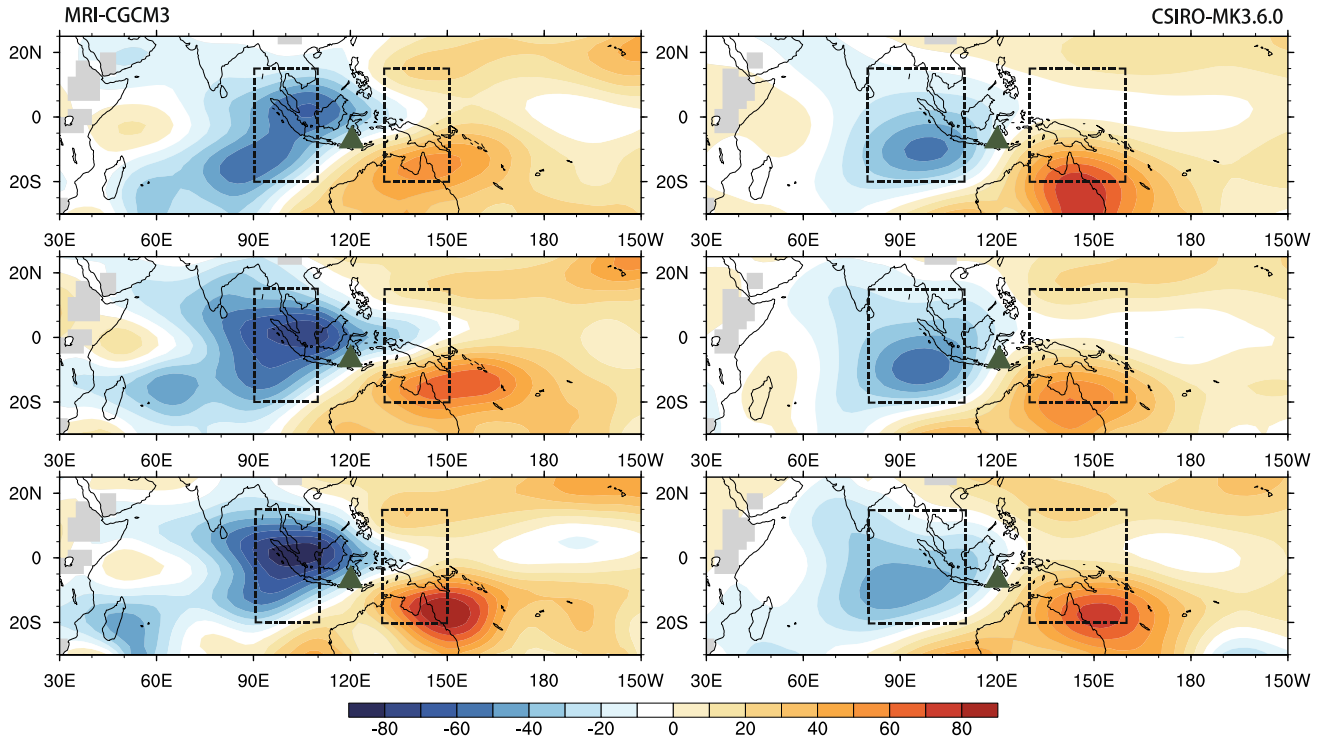

Fig. 14 Horizontal distributions of column-integrated (850–200 hPa) MSE tendency (unit: $m^2\ s^{-2}\ day^{-1}$) in (row 1, 2 and 3) 1 °C, 2 °C and 4 °C warming phase for (left) MRI-CGCM3 and (right) CSIRO-Mk3.6.0. The green triangles at 120°E represent the MJO convection centers, and the black boxes represent the east (20°S–15°N, 90°E–110°E for MRI-CGCM3, and 80°E–110°E for CSIRO-Mk3.6.0) and west (20°S–15°N, 130°E–150°E for MRI-CGCM3, and 130°E–160°E for CSIRO-Mk3.6.0) region for the calculation of MSE budget

Table 4 East–west asymmetry of column-integrated MSE tendency anomaly for MRI-CGCM3 and CSIRO-Mk3.6.0. Unit: $m^2\ s^{-2}\ day^{-1}$

Warming		1 °C	2 °C	4 °C
East–west asymmetry	MRI-CGCM3	62.1	65.7	80.8
	CSIRO-Mk3.6.0	49.1	54.1	58.2

ascending branch associated with the change of the Pacific Walker Circulation.

It is worth mentioning that there are controversy arguments about the role of the enhanced static stability in affecting MJO propagation. One argument is that an increase in the static stability would slow down the MJO eastward propagation (Adames et al. 2017b; Rushley et al. 2019), because the increase of the static stability would weaken the heating-induced circulation change, which

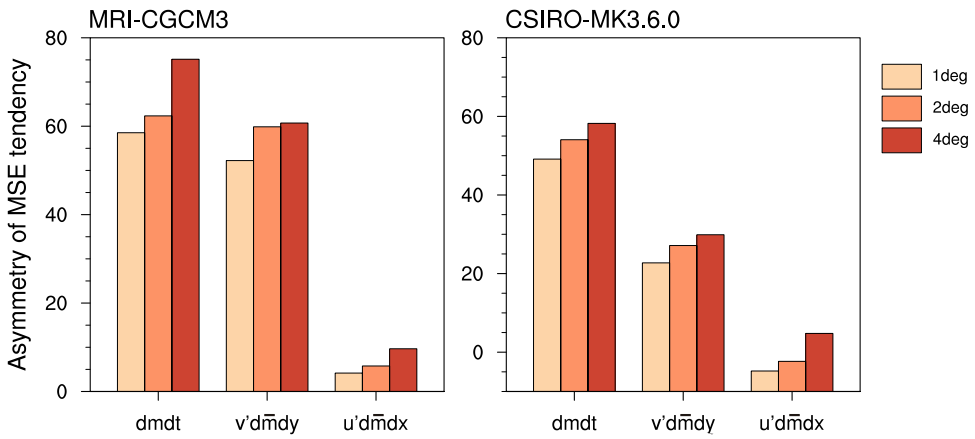

Fig. 15 East–west asymmetry of column-integrated MSE tendency anomaly ("dmdt"), the advection of mean MSE by anomalous meridional wind ("$v'\partial\bar{m}\partial y$") and by anomalous zonal wind ("$u'\partial\bar{m}\partial x$") for MRI-CGCM3 and CSIRO-Mk3.6.0. All anomalous fields were regressed against MJO-scale OLR anomaly over 15°S–5°S, 115°–125°E. Unit: $m^2\ s^{-2}\ day^{-1}$

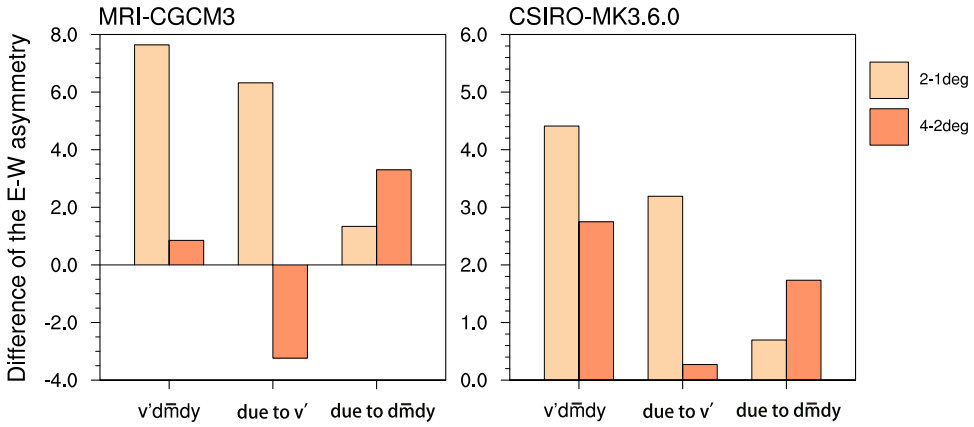

Fig. 16 Changes of east–west asymmetry of column-integrated advection of mean MSE by anomalous meridional wind from 1 to 2 °C warming phase (yellow) and from 2 to 4 °C warming phase (orange), and contributions to the asymmetry due to meridional wind field (the middle term) and mean MSE gradient (the right term) for MRI-CGCM3 and CSIRO-Mk3.6.0. Unit: $m^2\ s^{-2}\ day^{-1}$

Table 5 Percentage increase rate of MJO-related diabatic heating, static stability, the estimated and the actual MJO-related meridional wind in different warming phases for MRI-CGCM3 and CSIRO-Mk3.6.0

	$d\dot{Q}/\dot{Q}$ (%)	$d\sigma/\sigma$ (%)	Estimated dv/v (%)	Actual dv/v (%)
MRI-CGCM3				
1→2 deg	31	4.2	7.5	9.8
2→4 deg	3.2	6.0	−7.0	−3.7
CSIRO-Mk3.6.0				
1→2 deg	37.0	4.9	12.0	17.8
2→4 deg	15.4	8.1	1.6	6.0

would further result in a decrease in the horizontal MSE advection and thus a reduction of east–west asymmetry of the MSE tendency. By constructing a theoretical framework, we demonstrate that the net effect of the diabatic heating and the mean static stability changes lead to an enhanced MJO-scale circulation change, especially during the initial warming phase, which can have a positive impact on the zonal asymmetry of the MSE tendency. Another school of thinking is based on wave dynamics. An increase in the mean static stability causes the acceleration of internal gravity wave speed and thus the increase of equatorial Kelvin wave speed. If considering the MJO as a convectively coupled Kelvin wave (Wang 1988) or a Kelvin–Rossby wave couplet (Wang and Li 1994), an enhanced Kelvin wave would hasten the eastward phase speed of MJO (Wang et al. 2018). A further study is needed to reveal the relative role of the competing processes associated with the mean static stability change.

While CMIP5 models have been used to understand the future projection of MJO, caution is needed in interpreting the result because all the models possess systematic biases in the mean state and MJO simulations under the present-day climate condition. For example, the OLR spectrum in most of the models tends to shift toward higher wavenumbers compared to the observations while the zonal wind spectrum shows a more consistent feature with the observations with a clear peak at wavenumber 1. What causes such a bias in the models is unclear. It may be attributed

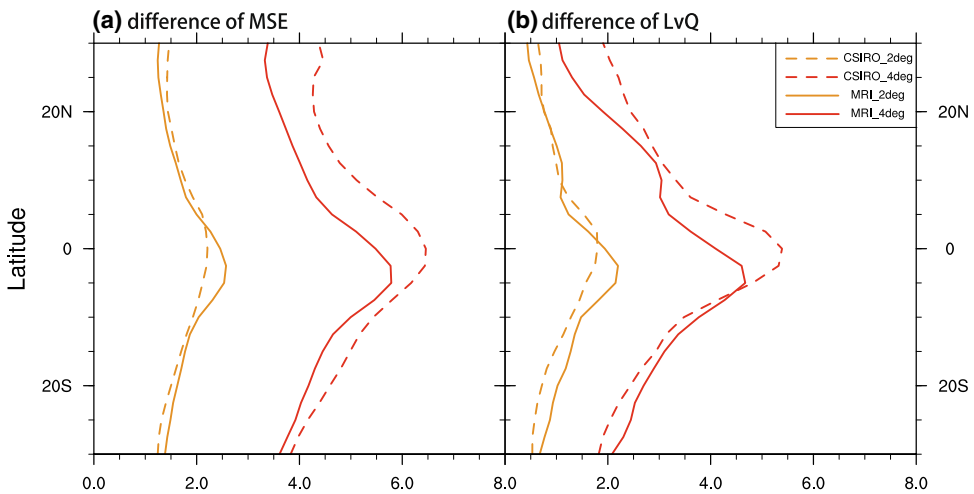

Fig. 17 Vertical profiles of differences of mean **a** MSE and **b** specific humidity (multiplied by L_v) averaged over 700–500 hPa (orange) between 2 and 1 °C warming phase and (red) between 4 and 1 °C warming phase for (solid line) MRI-CGCM3 and (dashed line) CSIRO-Mk3.6.0. Unit: $10^{-3}\ m^2/s^2$

to unrealistic convective parameterization. It is unclear to what extent such a bias would influence the future projection of MJO.

Acknowledgements JC would like to thank Lili Zhu for his help in data analysis and discussions. This work was jointly supported by China National Key R&D Program 2017YFA0603802 and 2015CB453200, NSFC Grants 41630423/41875069, NOAA NA18OAR4310298 and NSF AGS-1643297. This is SOEST Contribution No. 12345, IPRC Contribution No. 1387 and ESMC No. 262.

Appendix

A simple theoretical framework for understanding atmospheric low-level circulation response to a specified heating is the Gill (1980) model. Following the notation of Wang and Li (1993), the governing equations for a linear first-baroclinic mode shallow water model in an equatorial beta-plane with a longwave approximation may be written as:

$$\begin{cases} \varepsilon u - \beta y v = -\frac{\partial \emptyset}{\partial x} \\ \beta y u = -\frac{\partial \emptyset}{\partial y} \\ \varepsilon \emptyset + c^2 \nabla \cdot \vec{V} = -a\dot{Q} \end{cases} \tag{4}$$

where u, v, $\emptyset$ and $\dot{Q}$ represent MJO-scale zonal wind, meridional wind, geopotential and diabatic heating, ε is Rayleigh friction coefficient and c is the first-baroclinic gravity wave speed. Based on the momentum equation, u and v can be transformed into the function of $\emptyset$, that is,

$$\begin{cases} v = \frac{1}{\beta y}\left(\frac{\partial \emptyset}{\partial x} - \frac{\varepsilon}{\beta y}\frac{\partial \emptyset}{\partial y}\right) \\ u = -\frac{1}{\beta y}\frac{\partial \emptyset}{\partial y} \end{cases} \tag{5}$$

Let L_x be characteristic zonal length scale, and L_y be characteristic meridional length scale, which equals to the radius of Rossby deformation ($L_y = \sqrt{\frac{c}{\beta}}$). Thus, the thermodynamic equation in Eq. (4) can be written as:

$$\varepsilon \emptyset - \frac{c^2}{\beta L_y^2 L_x}\emptyset + \frac{2\varepsilon c^2}{\beta^2 L_y^4}\emptyset + \frac{\varepsilon c^2}{\beta^2 L_y^4}\emptyset = -a\dot{Q}. \tag{6}$$

Equation (6) may be written as:

$$\left(\frac{c}{L_x} - 4\varepsilon\right)\emptyset = a\dot{Q}. \tag{7}$$

Taking the logarithm at both sides of Eq. (7) and applying total differentiation at both sides of the equation, one may obtain

$$\frac{dc}{c - 4\varepsilon L_x} + \frac{d\emptyset}{\emptyset} = \frac{d\dot{Q}}{\dot{Q}}, \tag{8}$$

where "d" denotes the change between two equilibrium states or two warming phases.

Given the relationship between anomalous geopotential height and wind fields in Eq. (5), the change rate of the anomalous meridional wind may be written as:

$$\frac{dv}{v} = \frac{d\left(\beta L_y^2 - \varepsilon L_x\right)}{\beta L_y^2 - \varepsilon L_x} - \frac{d\left(\beta^2 L_y^3 L_x\right)}{\beta^2 L_y^3 L_x} + \frac{d\emptyset}{\emptyset}. \tag{9}$$

Equation (9) can be further simplified as

$$\frac{dv}{v} = \frac{dc}{c - \varepsilon L_x} - \frac{dc}{c} + \frac{d\emptyset}{\emptyset}. \tag{10}$$

Combining Eq. (5) and (10), one can obtain

$$\frac{dv}{v} = \frac{d\dot{Q}}{\dot{Q}} + \left(\frac{c}{c - \varepsilon L_x} - \frac{c}{\mathrm{c} - 4\varepsilon L_x} - 1\right)\frac{dc}{c}. \tag{11}$$

Given the relationship between the gravity wave speed c and the static stability σ:

$$c^2 = \frac{\sigma(\Delta p)^2}{2},$$

one may finally derive the following relation:

$$\frac{dv}{v} = \frac{d\dot{Q}}{\dot{Q}} + A\frac{d\sigma}{\sigma}, \tag{12}$$

where $A = \frac{1}{2}(1 - \frac{c}{c-\varepsilon L_x} + \frac{c}{c-4\varepsilon L_x})$, and Δp denotes half depth of the troposphere.

Equation (12) states that the percentage change of MJO-scale meridional wind is determined by the net effect of the increase rate of condensational heating associated with the increase of the mean moisture under global warming and the increase rate of the mean static stability in middle troposphere weighted by a parameter A.

References

Adames ÁF, Kim D, Sobel AH, Genio AD, Wu JB (2017a) Changes in the structure and propagation of the MJO with increasing CO_2. J Adv Model Earth Syst 9:1251–1268. https://doi.org/10.1002/2017MS000913

Adames ÁF, Kim D, Sobel AH, Genio AD, Wu JB (2017b) Characterization of moist processes associated with changes in the propagation of the MJO with increasing CO_2. J Adv Model Earth Syst 9:2946–2967. https://doi.org/10.1002/2017MS001040

Arnold NP, Kuang Z, Tziperman E (2013) Enhanced MJO-like variability at high SST. J Clim 26:988–1001. https://doi.org/10.1175/JCLI-D-12-00272.1

Arnold NP, Branson M, Kuang Z, Randall DA, Tziperman E (2015) MJO intensification with warming in the super-parameterized CESM. J Clim 28:2706–2724. https://doi.org/10.1175/JCLI-D-14-00494.1

Bi M, Li T, Shen X, Peng M (2015) To what extent the presence of real-strength tropical cyclones influences the estimation of atmospheric

intraseasonal oscillation intensity? Atmos Sci Lett 16:438–444. https://doi.org/10.1002/asl.579
Chang CWJ, Tseng WL, Hsu HH, Keenlyside N, Tsuang BJ (2015) The Madden–Julian oscillation in a warmer world. Geophys Res Lett 42:6034–6042. https://doi.org/10.1002/2015GL065095
Chen L, Li T, Wang B, Wang L (2017) Formation mechanism for 2015/16 Super El Niño. Sci Rep. https://doi.org/10.1038/s41598-017-02926-3
Diao Y, Li T, Hsu PC (2018) Influence of the boreal summer intraseasonal oscillation on extreme temperature events in the northern hemisphere. J Meteorol Res 32:534–547. https://doi.org/10.1007/s13351-018-8031-8
Fu B, Li T, Peng MS, Weng F (2007) Analysis of tropical cyclone genesis in the western North Pacific for 2000 and 2001. Weather Forecast 22:763–780. https://doi.org/10.1175/WAF1013
Gill AE (1980) Some simple solutions for heat induced tropical circulation. Q J R Meteorol Soc 106:447–462. https://doi.org/10.1002/qj.49710644905
Hendon HH, Salby ML (1994) The life cycle of the Madden–Julian oscillation. J Atmos Sci 51:2225–2237. https://doi.org/10.1175/1520-0469(1994)051%3c2225:TLCOTM%3e2.0.CO;2
Hendon HH, Zhang C, Glick JD (1999) Interannual variation of the Madden–Julian oscillation during austral summer. J Clim 12:2538–2550. https://doi.org/10.1175/1520-0442(1999)012<2538:IVOTMJ>2.0.CO;2
Hong C, Li T (2009) The extreme cold anomaly over Southeast Asia in February 2008: roles of ISO and ENSO. J Clim 22:3786–3801. https://doi.org/10.1175/2009JCLI2864.1
Hsu PC, Li T (2012) Role of the boundary layer moisture asymmetry in causing the eastward propagation of the Madden–Julian oscillation. J Clim 25:4914–4931. https://doi.org/10.1175/JCLI-D-11-00310.1
Hsu PC, Li T, You L, Gao J, Ren H (2014) A spatial–temporal projection model for 10–30 day rainfall forecast in South China. Clim Dyn 44:1227–1244. https://doi.org/10.1007/s00382-014-2215-4
Jiang X, Waliser D, Xacier PK, Petch J, Klingaman NP et al (2015) Vertical structure and physical processes of the Madden–Julian oscillation: exploring key model physics in climate simulations. J Geophys Res Atmos 120:4718–4748. https://doi.org/10.1002/2014JD022375
Kalnay E, Kanamitsu M, Kistler R, Collins W, Deaven D et al (1996) The NCEP/NCAR 40-year reanalysis project. Bull Am Meteorol Soc 77:437–472. https://doi.org/10.1175/1520-0477(1996)077<0437:TNYRP>2.0.CO;2
Lau WKM, Chan PH (1986) Aspects of the 40–50 day oscillation during the northern summer as inferred from outgoing longwave radiation. Mon Weather Rev 114:1354–1367. https://doi.org/10.1175/1520-0493(1986)114,1354:AOTDOD.2.0.CO;2
Lau WKM, Waliser DE (2011) Intraseasonal variability in the atmosphere–ocean climate system. Springer, Berlin
Lengaigne M, Guilyardi E, Boulanger JP, Menkes C, Delecluse P et al (2004) Triggering of El Niño by westerly wind events in a coupled general circulation model. Clim Dyn 23:601–620. https://doi.org/10.1007/s00382-004-0457-2
Li T (2014) Recent advance in understanding the dynamics of the Madden–Julian oscillation. Acta Meteorol Sin 28:1–33. https://doi.org/10.1007/s13351-014-3087-6
Li T, Wang B (1994) A thermodynamic equilibrium climate model for monthly mean surface winds and precipitation over the tropical Pacific. J Atmos Sci 51:1372–1385. https://doi.org/10.1175/1520-0469(1994)051%3c1372:ATECMF%3e2.0.CO;2
Li T, Zhou C (2009) Planetary scale selection of the Madden–Julian oscillation. J Atmos Sci 66:2429–2443. https://doi.org/10.1175/2009JAS2968.1
Liebmann B, Smith CA (1996) Description of a complete (interpolated) outgoing longwave radiation dataset. Bull Am Meteorol Soc 77:1275–1277
Liu P, Li T, Wang B, Zhang MH, Luo JJ et al (2013) MJO change with A1B global warming estimated by the 40-km ECHAM5. Clim Dyn 41:1009–1023. https://doi.org/10.1007/s00382-012-1532-8
Liu F, Zhou L, Ling J, Fu X, Huang G (2016) Relationship between SST anomalies and the intensity of intraseasonal variability. Theor Appl Climatol 124:847–854. https://doi.org/10.1007/s00704-015-1458-2
Madden RA, Julian PR (1972) Description of global-scale circulation cells in the tropics with a 40–50 day period. J Atmos Sci 29:1109–1123. https://doi.org/10.1175/1520-0469(1972)029%3c1109:DOGSCC%3e2.0.CO;2
Maloney ED (2009) The moist static energy budget of a composite tropical intraseasonal oscillation in a climate model. J Clim 22:711–729. https://doi.org/10.1175/2008JCLI2542.1
Maloney ED, Xie SP (2013) Sensitivity of tropical intraseasonal variability to the pattern of climate warming. J Adv Model Earth Syst 5:32–47. https://doi.org/10.1029/2012MS000171
Roundy PE, Frank WM (2004) Applications of a multiple linear regression model to the analysis of relationships between eastward- and westward-moving intraseasonal modes. J Atmos Sci 61:3041–3048. https://doi.org/10.1175/JAS-3349.1
Rushley SS, Kim D, Adames ÁF (2019) Changes in the MJO under greenhouse gas-induced warming in CMIP5 models. J Clim 32:803–821. https://doi.org/10.1175/JCLI-D-18-0437.1
Wang B (1988) Dynamics of tropical low-frequency waves: an analysis of the moist Kelvin wave. J Atmos Sci 45:2051–2065. https://doi.org/10.1175/1520-0469(1988)045%3c2051:DOTLFW%3e2.0.CO;2
Wang B, Li T (1993) A simple tropical atmosphere model of relevance to short-term climate variations. J Atmos Sci 50:260–284. https://doi.org/10.1175/1520-0469(1993)050%3c0260:ASTAMO%3e2.0.CO;2
Wang B, Li T (1994) Convective interaction with boundary-layer dynamics in the development of a tropical intraseasonal system. J Atmos Sci 51:1386–1400. https://doi.org/10.1175/1520-0469(1994)051%3c1386:CIWBLD%3e2.0.CO;2
Wang B, Rui H (1990) Dynamics of the coupled moist Kelvin–Rossby wave on an equatorial β-plane. J Atmos Sci 47:397–413. https://doi.org/10.1175/1520-0469(1990)047%3c0397:DOTCMK%3e2.0.CO;2
Wang L, Li T, Maloney E, Wang B (2017) Fundamental causes of propagating and non-propagating MJOs in MJOTF/GASS models. J Clim 30:3743–3769. https://doi.org/10.1175/JCLI-D-16-0765.1
Wang L, Li T, Nasuno T (2018) Impact of Rossby and Kelvin wave components on MJO eastward propagation. J Clim 31:6913–6931. https://doi.org/10.1175/JCLI-D-17-0749.1
Wheeler MC, Hendon HH (2004) An all-season real-time multivariate MJO index: development of an index for monitoring and prediction. Mon Weather Rev 132:1917–1932. https://doi.org/10.1175/1520-0493(2004)132%3c1917:AARMMI%3e2.0.CO;2
Wheeler M, Kiladis GN (1999) Convectively coupled equatorial waves: analysis of clouds and temperature in the wavenumber–frequency domain. J Atmos Sci 56:374–399. https://doi.org/10.1175/1520-0469(1999)056%3c0374:CCEWAO%3e2.0.CO;2
Zhao CB, Li T, Zhou T (2013) Precursor signals and processes associated with MJO initiation over the tropical Indian Ocean. J Clim 26:291–307. https://doi.org/10.1175/JCLI-D-12-00113.1
Zhu Z, Li T, Hsu PC, He J (2015) A spatial–temporal projection model for extended-range forecast in the tropics. Clim Dyn 45:1085–1098. https://doi.org/10.1007/s00382-014-2353-8